Journal of Magnetic Resonance **139,** 35–45 (1999)
Article ID jmre.1999.1744, available online at http://www.idealibrary.com on IDEAL®

# Experimental Evaluation of a Surface Charge Method for Computing the Induced Magnetic Field in Trabecular Bone

Scott N. Hwang and Felix W. Wehrli

*University of Pennsylvania Medical Center, Department of Radiology, Philadelphia, Pennsylvania 19104*

Received March 27, 1998; revised January 20, 1999

**The magnetic field induced in the pores of trabecular bone as a result of the susceptibility difference between bone and bone marrow was computed with the aid of magnetic surface charge models generated from images of trabecular bone specimens acquired at 78 and 63 $\mu$m resolution. The predicted field was compared with the values derived from 2D and 3D field maps obtained by echo-offset imaging techniques and excellent agreement was found between the two methods. Finally, from the slopes of regression between the experimental and computed fields, the absolute susceptibility of bone was nondestructively determined as $-11.0 \times 10^{-6}$ (MKS), which is in close agreement with a reported value of $-11.3 \times 10^{-6}$ obtained with powdered bone by means of a spectroscopic susceptibility matching technique (J. A. Hopkins and F. W. Wehrli,** *Magn. Reson. Med.* **37, 494–500 (1997)).** 

*Key Words:* **trabecular bone; magnetic susceptibility; induced magnetic field; magnetic field computation; magnetic field measurement.**

## INTRODUCTION

Osteoporosis is a disease characterized by a loss of bone mass. As a result, bone density has been the chief criterion for noninvasively assessing bone quality. Although low bone density increases the risk of fracture (*1–4*), there is evidence that inclusion of parameters quantifying trabecular architecture significantly improves predictability. For example, Kleerekoper *et al.* (*5*) and Recker *et al.* (*6*) have shown by histomorphometry of biopsies that in subjects matched for bone density, those with vertebral deformity had significant differences in trabecular architecture, including lower trabecular plate density, increased trabecular separation, and increased trabecular thickness. However, bone biopsies are invasive and therefore impractical for repeated monitoring of osteoporotic subjects. The limitations of current methods have spurred the investigation of alternative means by which MRI can be applied to noninvasively assess trabecular architecture. The direct strategy relies on the acquisition of high-resolution images of trabecular bone followed by image analysis in a manner analogous to traditional histomorphometry (*7, 8*). The potential of this method has recently been demonstrated with structural parameters derived from MR images acquired *in vivo* showing significant correlation with the presence of vertebral deformities (*9*).

However, MR images of sufficient resolution for direct analysis can only be obtained at a peripheral site, such as the radius or calcaneus. MRI offers another means by which trabecular structure can be quantified at any anatomic location without the need to resolve individual trabeculae. This second method is based on measuring the field inhomogeneities which result from the different magnetic susceptibilities of bone and marrow (*10, 11*). The discontinuity in the magnetic properties induces magnetic field perturbations, which increase the rate of NMR relaxation. Since the degree of field inhomogeneity depends upon the geometry of the bone/marrow surface, the relaxation rate provides an indirect measure of trabecular architecture.

For the purpose of investigating the effect of structure on the susceptibility-induced field, several investigators resorted to model lattices mimicking, for example, the airways in the lungs (*12, 13*) or the trabeculae in bone (*14*). Applying a statistical approach to treat trabeculae as a continuum of infinitely long oriented rods, a theoretical relationship between the NMR signal and geometrical parameters was established (*15*) and experimentally verified (*16, 17*). In a very different approach aimed at investigating the effects of realistic structures on the induced field, the present authors invoked a surface charge method for calculating the susceptibility-induced magnetic field on the basis of surfaces generated from high-resolution 3D MR images (*18*).

The purpose of the current work was to evaluate the accuracy of the surface models derived from MR images of trabecular bone specimens by comparing the computed induced field with measured values determined by 2D and 3D MR phase mapping techniques. A byproduct of the analysis is a means of nondestructively measuring the magnetic susceptibility of trabecular bone and other materials forming complex structures.



1090-7807/99 $30.00

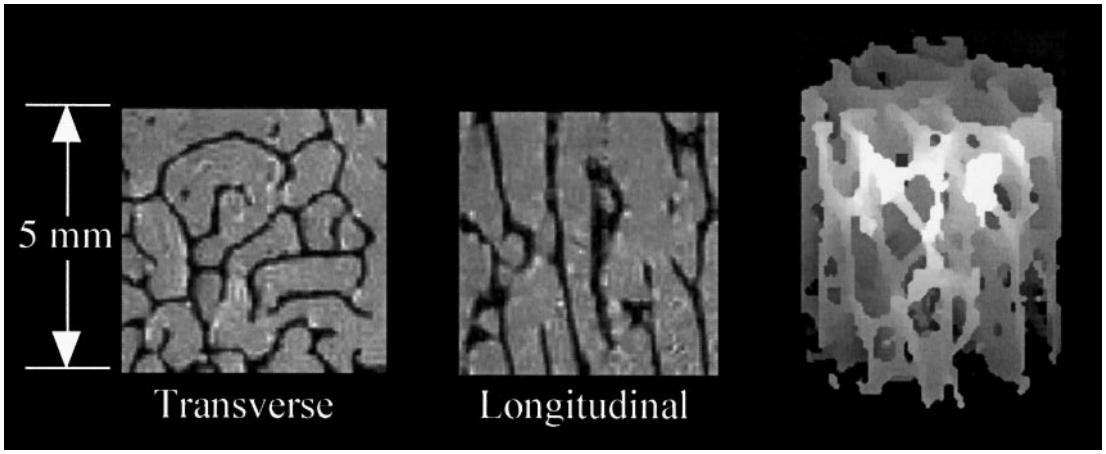


**FIG. 1.** Cross sectional and projection images of the 3D MR data set ($78 \times 78 \times 78$ $\mu m^3$ voxels) acquired from the human bone specimen.

## METHODS

### *3D Imaging*

A cylindrical specimen (9-mm diameter and length) of trabecular bone from the human distal radius was harvested from a frozen cadaver (Fig. 1). An additional specimen was obtained from the distal femur of a rabbit (Fig. 2). The two specimens were chosen for their sharply contrasting structures. The thick trabeculae of the rabbit specimen are packed closely together while the human specimen is characterized by slender trabeculae which are widely spaced. The bone marrow was removed by immersing the cores in an ultrasonic bath of trichloroethylene for 4 h, followed by rinsing with a water pick. To optimize the signal-to-noise ratio, the human and rabbit specimens were suspended in water doped with 1.0 and 1.2 mM Gd-DTPA, respectively, to increase the longitudinal relaxation rate to $\sim 3\ s^{-1}$. The magnetic field inhomogeneities resulting from the susceptibility discontinuity at the air/sample interface were minimized by imaging the rabbit specimen in a Shigemi tube (8-mm outer diameter, Shigemi, Inc., Tokyo, Japan) in which the specimen was enclosed above and below by layers of glass that were susceptibility-matched to water. The human specimen was imaged in a typical flat-bottom glass test tube since a Shigemi tube of sufficient diameter was not available.

3D MR images of the human specimen ($78 \times 78 \times 78$ $\mu m^3$ voxels) and the rabbit specimen ($63 \times 63 \times 63$ $\mu m^3$ voxels) were obtained with a Bruker AM-400 9.4 T 89-mm-bore spectrometer/microimaging system. The cores were imaged using commercial RF coil inserts and the RASEE partial flip-angle spin-echo pulse sequence (*19*). Matrix size was $128 \times 128 \times 128$ and pulse repetition time and echo time were 100 and 6 ms, respectively. Both specimens were imaged with their anatomic axes parallel to the direction of the applied magnetic field (Figs. 1 and 2). The rabbit specimen was also imaged with its axis perpendicular to the field.

### *Phase Mapping*

As in previous work investigating the induced field distribution in trabecular bone of the human lumbar spine (*20*), the modified spin-echo pulse sequence (*21, 22*) diagrammed in Fig. 3 was applied to spatially map the magnetic field in a cross section of the radius specimen. Since a Shigemi tube was not available, data were collected near the center of the specimen in order to avoid the strongest background gradients. In addition, data for the phase maps were collected at twice the voxel size ($78 \times 78 \times 156$ $\mu m^3$) as that of the 3D image in order to improve the signal-to-noise ratio.

In a spin-echo pulse sequence, the gradient and radiofrequency (RF) echoes are usually coincident ($T_{rf} = T_{ge}$) so that all isochromats are completely rephased. However, it is well known that if the 180° RF pulse is applied at a time offset $\tau > 0$ earlier, the magnetization rephases at time $T_{ge} - 2\tau$ and accumulates an extra phase shift $\phi = 2\gamma B_z^{rot}\tau$ which, in the absence of other field offsets, is proportional to the susceptibility-induced local flux density $B_z^{rot}$ in the rotating frame of reference. The phase can then be spatially mapped in the resulting image as the complex argument of the signal in each voxel:

$$\phi[\mathbf{r}] = \tan^{-1}(I[\mathbf{r}]/R[\mathbf{r}]), \qquad [1]$$

where $I$ and $R$ represent the imaginary and real components of the complex magnetization, and $\mathbf{r}$ is the voxel's spatial location. The field in each voxel is then computed as $B_z^{rot}[\mathbf{r}] = \phi[\mathbf{r}]/(2\gamma\tau)$. In practice, $B_z^{rot}$ is calculated from the phases measured for two different 180° pulse offsets, $\tau_1$ and $\tau_2$, to cancel out systematic phase errors:

$$\Delta\phi[\mathbf{r}] = \phi(\tau_2, [\mathbf{r}]) - \phi(\tau_1, [\mathbf{r}]) = \gamma B_z^{rot}[\mathbf{r}]2\Delta\tau \qquad [2]$$

$$B_z^{rot}[\mathbf{r}] = \Delta\phi[\mathbf{r}]/(\gamma 2\Delta\tau). \qquad [3]$$

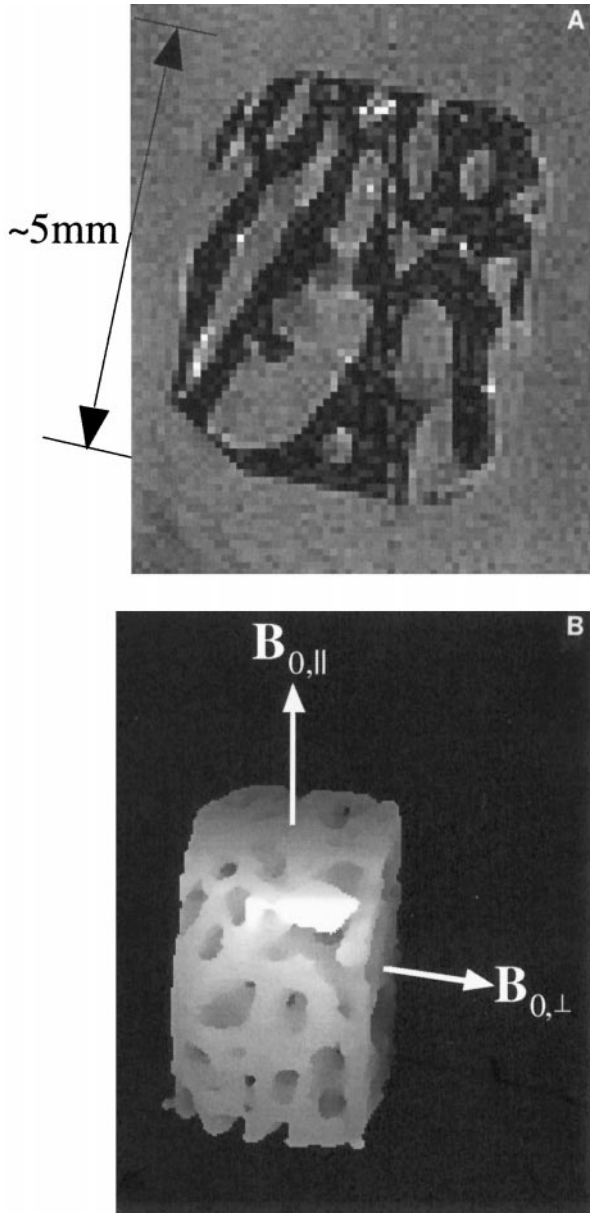


**FIG. 2.** A cross sectional slice (A, 63 × 63 × 63 $\mu m^3$ voxels) and 3D projection image (B) of the rabbit specimen used for 3D validation of the field computations. Phase maps were generated with the anatomic axis parallel ($\mathbf{B}_{0,||}$) and perpendicular ($\mathbf{B}_{0,\perp}$) to the applied field $\mathbf{B}_0$.

For the cross section of the human specimen, the field $B_z^{rot}[\mathbf{r}]$ in each voxel was calculated from phase maps obtained with $\tau_1 = 0$ ms and $\tau_2 = 0.5$ ms.

For purposes of mapping the field within the entire volume of the rabbit bone, a 3D version (*23*) of the RASEE partial flip-angle spin-echo technique (*24*) was also made phase-sensitive by allowing the 180° RF pulse to be offset. RASEE represents the spin-echo counterpart of the partial-flip angle gradient echo in that addition of a phase-reversal RF pulse

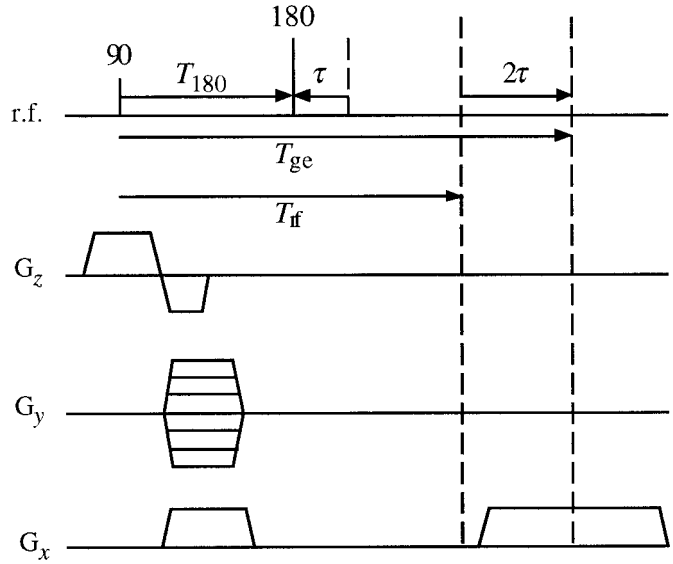


**FIG. 3.** 2D spin-echo pulse sequence used for acquiring phase maps in the human specimen.

demands that the flip angle $\alpha$ of the excitation pulse be replaced by its 180° complement. Since selective pulses of large nutation angle are difficult to achieve, RASEE uses a composite pulse consisting of a nonselective 180° pulse followed by a slice-selective $\alpha$ pulse. The pulse sequence uses rewinder gradients on *y* and *z* (Fig. 4). Data were collected with the anatomic axis of the specimen parallel and then perpendicular

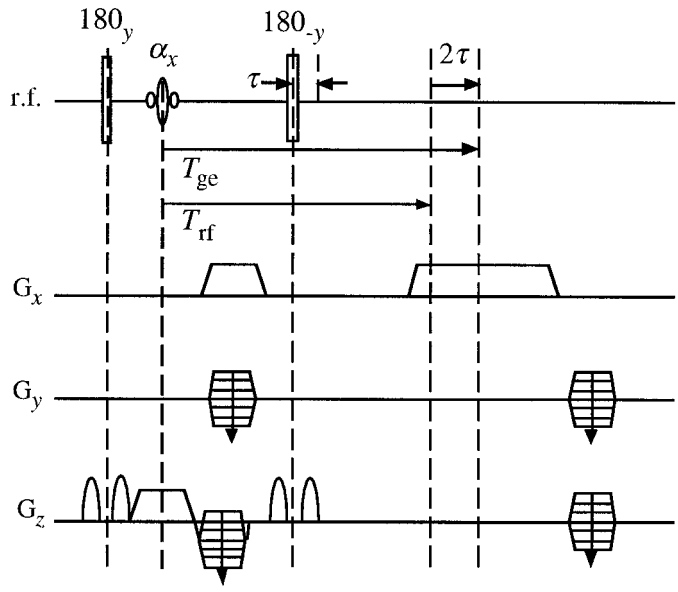


**FIG. 4.** Phase-sensitive 3D RASEE pulse sequence as described in the text. The pulse sequence is identical to the one described by Jara *et al.* (*23*) except that the location of the phase-reversal pulse was made variable to produce a phase shift from which field maps can be constructed.

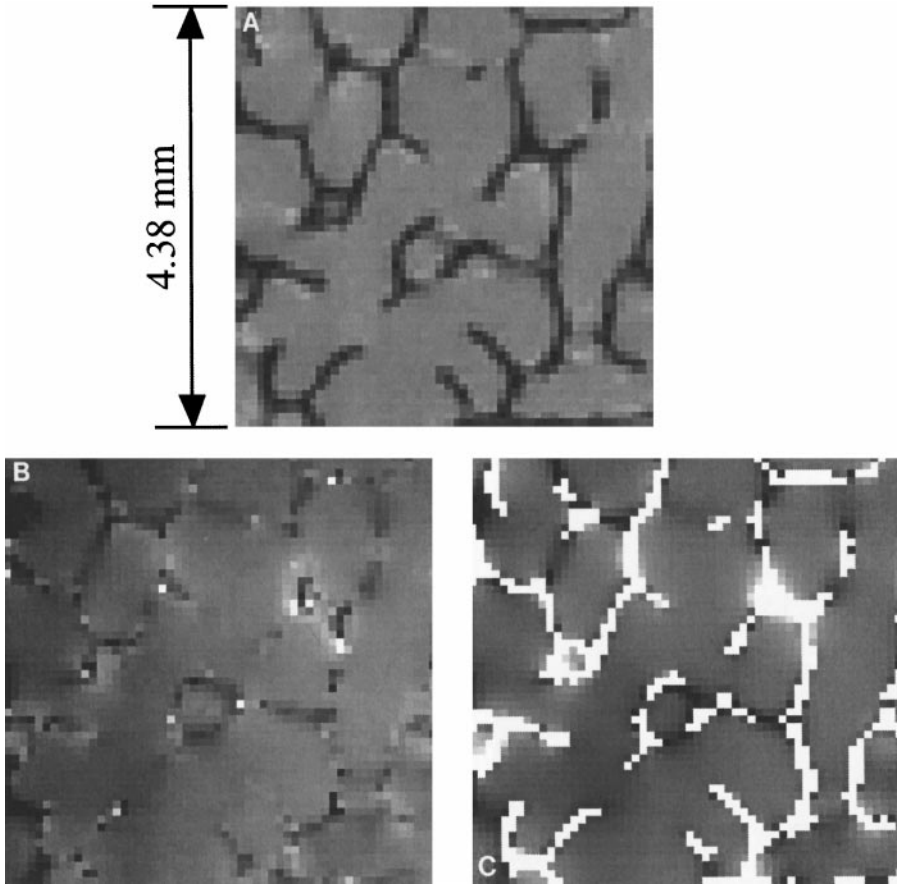


**FIG. 5.** Maps of the measured (B) and predicted (C) induced field values for each voxel ($78 \times 78 \times 156$ $\mu m^3$) shown in the magnitude image (A) of the human radius trabecular bone. In (B), the voxels with ≥50% bone are displayed in white. Dark intensities in (B) and (C) indicate regions where the induced field is more negative. Note that the field is more perturbed in regions near trabeculae.

to the applied field $B_0$ (Fig. 2). For each spatial orientation, the specimen was imaged twice ($128 \times 128 \times 128$ voxel$^3$ resolution, $63 \times 63 \times 63$ $\mu m^3$ voxel size) with $\tau_1 = 0$ ms and $\tau_2 = 0.5$ ms. The anatomic image shown in Fig. 2 is from an image acquired with $\tau_1 = 0$ ms and with the specimen in the parallel orientation. The field, $B_z^{rot}[\mathbf{r}]$, was spatially mapped on the basis of each pair of images.

*Computing the Induced Field*

The field was computed by the surface charge method on the basis of the 3D images. The calculations were performed on a Toshiba Satellite 225CDS laptop computer (133 MHz Pentium). Surface models of trabecular bone were generated by the triangulation algorithm described previously (*18*). Prior to surface triangulation, a $3 \times 3$ median filter was applied to each slice of the rabbit images to reduce noise. Since the trabeculae of the rabbit specimen were thick in comparison to voxel size, the histogram of voxel intensities exhibited distinct bone and marrow peaks. Therefore, the intensity threshold for classifying voxels as bone or marrow in the triangulation algorithm was set to the average of the two peak locations in the histogram. Since the trabeculae in the human specimen were more slender with respect to voxel size, the maximum-likelihood bone volume fraction was computed in each voxel to minimize misclassification errors (*25*). Voxels that were ≥50% bone were classified as bone for the purpose of generating a surface model. For both specimens, false trabeculae resulting from noise-induced misclassification errors were removed by applying a depth-first search algorithm (*26*) to find all the "islands" of bone. Under the assumption that isolated islands do not exist, the voxels of any island that were not connected to the outer limits of the volume of interest were reclassified as pure marrow. The surface model for the human specimen consisted of 179,340 triangles while those generated from the images of the rabbit specimen with the anatomic axis parallel and perpendicular to the applied field were composed of 150,010 and 146,512 triangles, respectively.

After generating a surface model, a normalized surface charge density, $\tilde{\sigma}$, was computed for each triangle:

$$\tilde{\sigma} = \frac{\sigma}{H_0 \Delta\chi} \approx \mu_0 \cos(\alpha), \qquad [4]$$

where $\sigma$ is the charge density, $H_0$ is the magnitude of the static field intensity, $\Delta\chi$ is the susceptibility difference $\chi_{\text{bone}} - \chi_{\text{Gd-DTPA}}$, and $\alpha$ is the angle between the static field and the surface normal pointing from the bone surface into marrow. By integrating over the surface, $S'$, a dimensionless normalized induced field intensity, $\mathbf{h}_{\text{induced}}$, was subsequently calculated:

$$\mathbf{h}_{\text{induced}} = \frac{\mathbf{H}_{\text{induced}}}{H_0 \Delta\chi} = \frac{1}{4\pi\mu_0} \oint_{S'} \tilde{\sigma}(\mathbf{r}') \frac{(\mathbf{r} - \mathbf{r}')}{|\mathbf{r} - \mathbf{r}'|^3} \, dA'. \qquad [5]$$

Rather than merely summing the field contribution from each triangle, the surface integral for the induced field was efficiently estimated by a multipole-accelerated algorithm which replaces large numbers of triangles with a multipole expansion of only 10 terms (*18*, *27*).

The total field intensity is the sum of the applied static field intensity, $\mathbf{H}_0 = \mathbf{B}_0/\mu_0$, and the induced field intensity, $\mathbf{H}_{\text{induced}}$:

$$\mathbf{H}(\mathbf{r}) = \mathbf{H}_0 + \mathbf{H}_{\text{induced}}(\mathbf{r}). \qquad [6]$$

The flux density is then given by

$$\begin{aligned} \mathbf{B}(\mathbf{r}) &= \mu(\mathbf{H}_0 + \mathbf{H}_{\text{induced}}(\mathbf{r})) \\ &= \mu_0(1 + \chi(\mathbf{r}))(\mathbf{H}_0 + \mathbf{H}_{\text{induced}}(\mathbf{r})) \\ &= (1 + \chi(\mathbf{r}))\mathbf{B}_0 + \mu_0(1 + \chi(\mathbf{r}))\mathbf{H}_{\text{induced}}(\mathbf{r}), \end{aligned} \qquad [7]$$

where $\chi$ is the susceptibility of the medium, i.e., the fluid in the marrow spaces.

The local field was computed by assuming the "sphere of Lorentz" approximation (*28*, *29*) and then substituting with Eq. [7]:

$$\begin{aligned} \mathbf{B}_{\text{loc}} &\approx \mathbf{B} - \frac{2\mu_0\mathbf{M}}{3} = \mathbf{B} - \frac{2\mu_0\chi\mathbf{H}}{3} \\ &= \mathbf{B} - \frac{2\chi\mathbf{B}}{3(1+\chi)} = \left(1 - \frac{2\chi}{3(1+\chi)}\right)\mathbf{B} \end{aligned} \qquad [8]$$

$$\mathbf{B}_{\text{loc}} = \mathbf{B}_0 + \frac{\chi}{3}\mathbf{B}_0 + \mu_0\left(1 + \frac{\chi}{3}\right)\mathbf{H}_{\text{induced}}. \qquad [9]$$

Finally, the local flux density in the rotating frame is given by

$$\begin{aligned} \mathbf{B}^{\text{rot}} = \mathbf{B}_{\text{loc}} - \mathbf{B}_0 &= \frac{\chi}{3}\mathbf{B}_0 + \mu_0\left(1 + \frac{\chi}{3}\right)\mathbf{H}_{\text{induced}} \\ &= \frac{\chi}{3}\mathbf{B}_0 + \mu_0\left(1 + \frac{\chi}{3}\right)H_0\Delta\chi\mathbf{h}_{\text{induced}} \\ &= \frac{\chi}{3}\mathbf{B}_0 + B_0\left(1 + \frac{\chi}{3}\right)\Delta\chi\mathbf{h}_{\text{induced}}. \end{aligned} \qquad [10]$$

*Magnetic Susceptibilities of Gadolinium-Doped Water and Bone*

The susceptibility and susceptibility difference must be known in order to compute $\mathbf{B}^{\text{rot}}$ using Eq. [10]. The susceptibility of bone has recently been reported as $\chi_{\text{bone}} = -4\pi 0.90 \times 10^{-6} = -11.3 \times 10^{-6}$ (MKS) (*30*). The MKS volume susceptibility of 1.2 mM Gd-DTPA was estimated as a weighted sum of susceptibilities (*29*),

$$\chi = 4\pi \sum_k c_k \chi_{M,k}, \qquad [11]$$

where $c_k$ is the concentration of species $k$ in mol/mL, and $\chi_{M,k}$ is the CGS molar susceptibility of species $k$ in mL/mol. The standard value for the molar susceptibility of water is $12.97 \times 10^{-6}$ mL/mol (CGS) (*31*). Since the concentration of Gd-DTPA was very small, the concentration of water was estimated from its molecular mass and density (*32*), i.e., (1.000 g/mL)/(18.02 g/mol) = 0.05549 mol/mL. For the current study, a value of $0.0256 \times 10^{-6}$ mL/mol (*33*) was used for the molar susceptibility of Gd-DTPA. This value is in close agreement with other values found in the literature (*34*, *35*). The volume susceptibility for 1.2 mM Gd-DTPA was then computed as

$$\begin{aligned} \chi_{1.2\text{ mM Gd-DTPA}} = 4\pi\Bigg\{ & 0.05549 \frac{\text{mol } H_2O}{\text{mL}} \\ & \times \left(-12.97 \times 10^{-6} \frac{\text{mL}}{\text{mol } H_2O}\right) \\ & + 1.2 \times 10^{-6} \frac{\text{mol Gd-DTPA}}{\text{mL}} \\ & \times \left(0.0256 \frac{\text{mL}}{\text{mol Gd-DTPA}}\right)\Bigg\}, \\ = -4\pi \times 0.689 \times 10^{-6} & \end{aligned} \qquad [12]$$

which provides a susceptibility difference of $\Delta\chi = \chi_{\text{bone}} - \chi_{1.2\text{ mM Gd-DTPA}} = -2.7 \times 10^{-6}$. Similarly, for 1.0 mM Gd-DTPA $\chi_{1.0\text{ mM Gd-DTPA}} = -4\pi \times 0.694 \times 10^{-6}$ and $\Delta\chi = \chi_{\text{bone}} - \chi_{1.0\text{ mM Gd-DTPA}} = -2.6 \times 10^{-6}$.

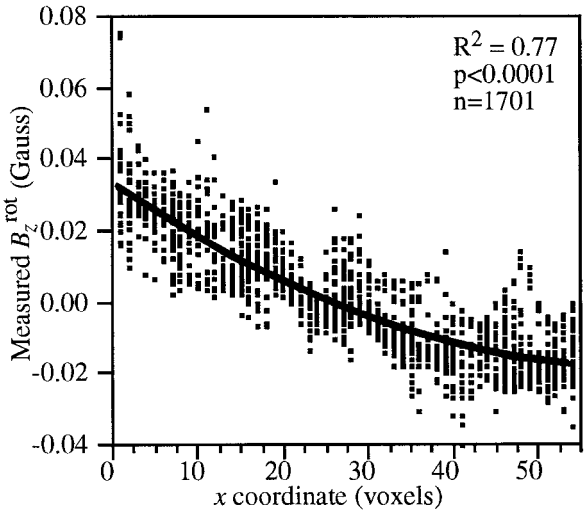


**FIG. 6.** The measured field in the human specimen was significantly correlated with the $x$ coordinate, indicating the presence of large-scale background gradients. Regression was performed with a second-order function of $x$: $B_z^{\text{rot}}[x] = a + bx + cx^2$.

### *Evaluation of the Surface Charge Method and Nondestructive Determination of Susceptibility*

The measured field was compared to the field predicted by the effective surface charge method. The $z$ component of the normalized field $h_{\text{induced},z}[\mathbf{r}]$ was computed at spatial locations corresponding to the centers of marrow voxels in the measured field maps. Regression was then performed between the measured field, $B_z^{\text{rot}}[\mathbf{r}]$, and the predicted field, $h_{\text{induced},r}[\mathbf{r}]$. According to Eq. [10], the apparent susceptibility difference may be computed from the slope, $m$, of the regression as

$$\Delta\chi = m/(B_0(1 + \chi_{\text{Gd-DTPA}}/3)) \approx m/B_0. \qquad [13]$$

The surface charge method, together with MR phase mapping, thus provides a nondestructive means of measuring the susceptibility of trabecular bone and other materials forming complex structures. In contrast, the previously reported value for the susceptibility of bone (*30*) was determined by a susceptibility-matching technique, which required the specimen to be ground into powder.

Since only short-range fields induced by trabecular bone were computed by the surface charge method, additional terms, $g[\mathbf{r}]$, were included in the regression models to account for background gradients (e.g., those caused by the susceptibility difference between the sample and surrounding air):

$$B_z^{\text{rot}}[\mathbf{r}] = mh_{\text{induced},z}[\mathbf{r}] + g[\mathbf{r}] + K, \qquad [14]$$

where $K$ represents a spatially uniform field offset. In regard to the rabbit specimen, for example, a first-order model with linear background gradients was expressed by

$$g[\mathbf{r}] = G_x x + G_y y + G_z z, \qquad [15]$$

where $G_x$, $G_y$, and $G_z$ were fitted parameters in addition to the coefficient $m$ and offset $K$. Likewise, the second-order model for the human specimen was given by

$$g[\mathbf{r}] = G_x x + G_{xx}x^2 + G_y y + G_{yy}y^2. \qquad [16]$$

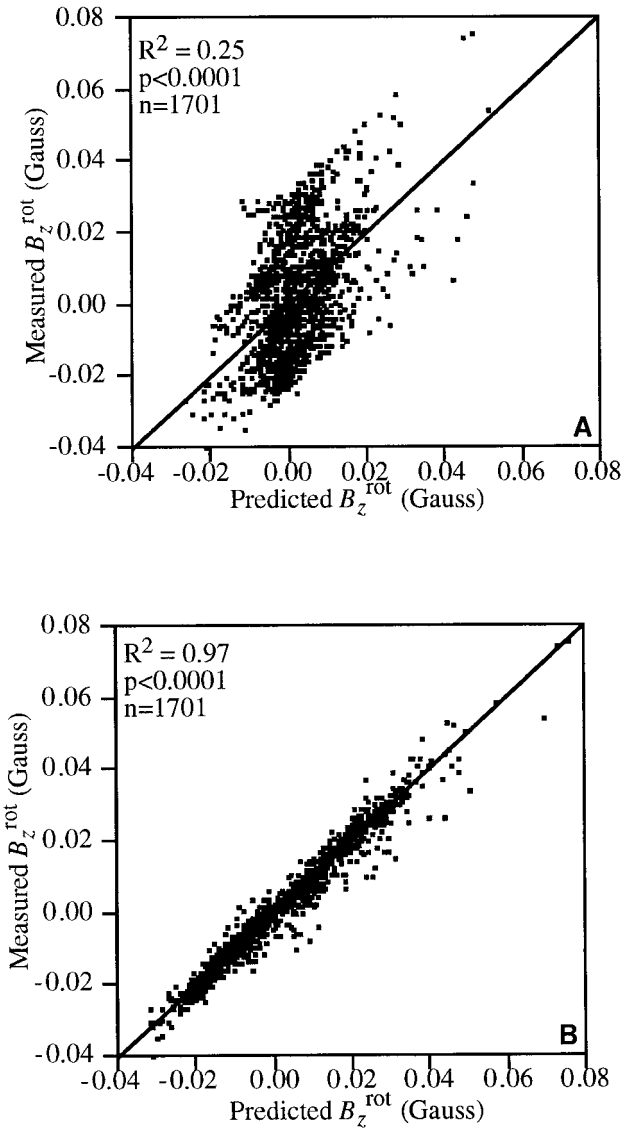


**FIG. 7.** The measured field versus the field predicted by a regression model with no terms (A) and with up to second-order terms (B) for background field gradients.

**TABLE 1**
**Determination of $\Delta\chi$ by Regression between the Measured and Predicted Field ($n = 1701$) for the Human Specimen**

| Order of background terms | $R^2$ | $p$ | $\Delta\chi$ | 95% Confidence interval for $\Delta\chi$ | |
|---|---|---|---|---|---|
| | | | | Lower | Higher |
| 0 | 0.25 | <0.0001 | $2.73 \times 10^{-6}$ | $2.50 \times 10^{-6}$ | $2.96 \times 10^{-6}$ |
| 1 | 0.90 | <0.0001 | $2.14 \times 10^{-6}$ | $2.05 \times 10^{-6}$ | $2.23 \times 10^{-6}$ |
| 2 | 0.97 | <0.0001 | $2.17 \times 10^{-6}$ | $2.12 \times 10^{-6}$ | $2.22 \times 10^{-6}$ |
| 3 | 0.97 | <0.0001 | $2.14 \times 10^{-6}$ | $2.09 \times 10^{-6}$ | $2.20 \times 10^{-6}$ |

The regression models for the human specimen were only functions of $x$ and $y$ since the field was evaluated in one cross section only.

## RESULTS AND DISCUSSION

### *Human Specimen*

The measured and predicted field maps for the human specimen are shown in Fig. 5. As described previously, the field was only measured in one cross section near the center of the specimen in order to avoid the strongest background gradients. The phase maps were also generated from data acquired with voxel size larger than the images used for surface triangulation to improve the signal-to-noise ratio. In spite of these measures, the measured field was more highly correlated with the $x$ coordinate than with the computed field (Figs. 6 and 7A), since the strongest background gradients were approximately in the $x$ direction (Fig. 5B). Nevertheless, the measured and predicted field maps look qualitatively similar (Fig. 5). Furthermore, as shown by the results in Table 1 and Fig. 7B, a combination of the computed field and a second-order model for the background gradients resulted in an excellent fit ($R^2 = 0.97$). To avoid unnecessary terms, an increase in the order of the regression model was rejected if it did not significantly improve

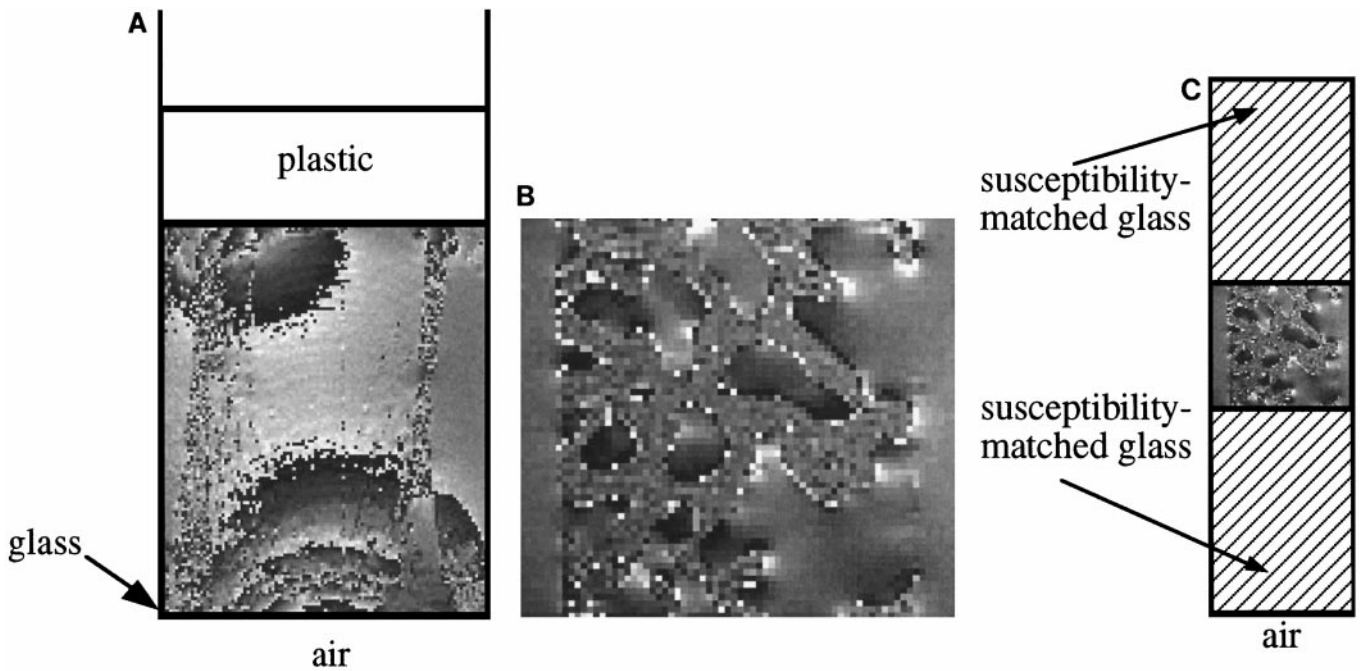


**FIG. 8.** (A) The severe phase distortions in the phase map of a specimen in a normal glass flat-bottom test tube result from the susceptibility difference between air and the sample and the finite length of the cylinder. (B) The distortions are not evident in a longitudinal cross section of a phase map measured from the rabbit femur since, as shown in (C), the specimen was sandwiched between two layers of glass matched to the susceptibility of water. The specimen was thus sufficiently removed from field perturbations caused by the susceptibility difference between glass and air. The phase map appears as random noise at locations in bone, where the NMR signal is negligible.

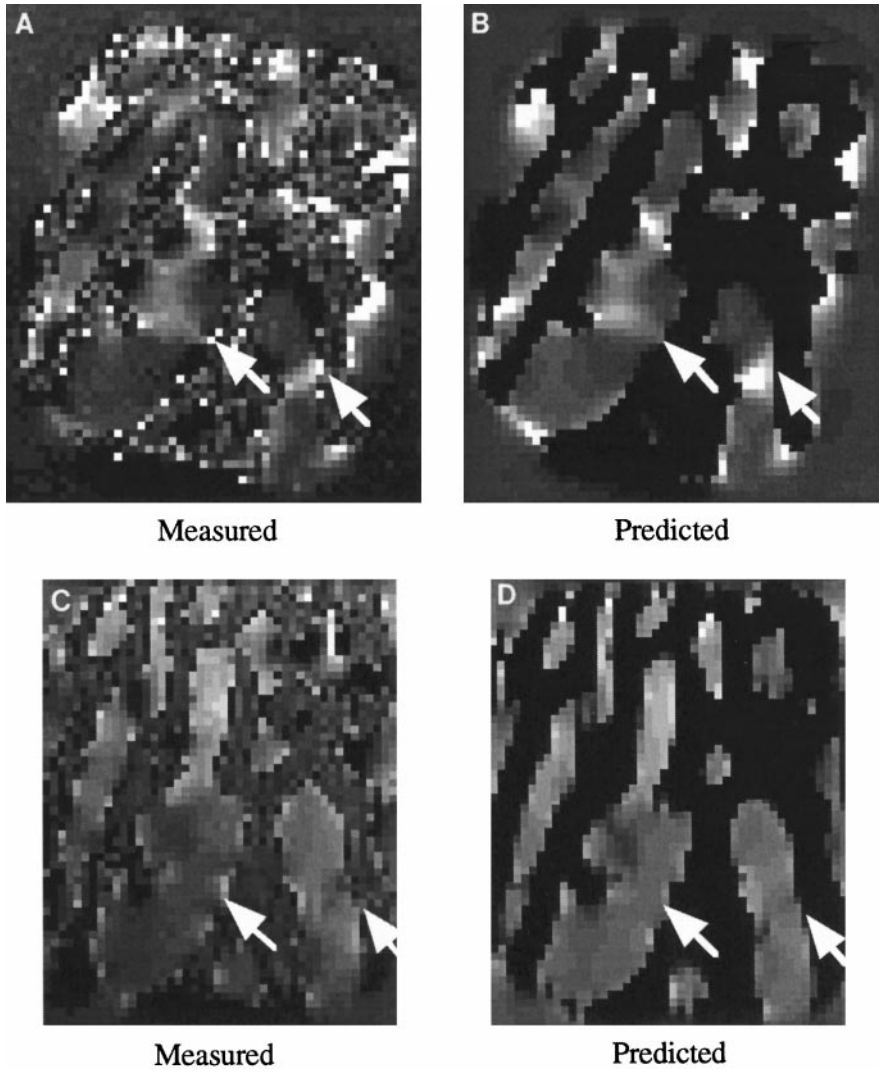


**FIG. 9.** Cross sections of the measured and predicted field maps with the specimen parallel (A, B) and perpendicular (C, D) to the applied field. The sections in (C) and (D) are approximately in the same plane relative to the specimen as those in (A) and (B). In contrast to Fig. 5, brighter intensities indicate regions where the induced field was more negative. The gray scale was inverted to make the field perturbations, indicated by the white arrows in (A) and (B), more distinct. Trabeculae in adjacent slices caused the inhomogeneities since they were perpendicular to the applied field, which is directed into the page for (A) and (B). Note that the field is more homogeneous at the locations indicated by arrows in (C) and (D) since the trabeculae were rotated to an orientation nearly parallel to the applied field, which is directed toward the right side of the page.

the $R^2$ correlation coefficient of the fit. Therefore, the susceptibility difference $\Delta\chi = -2.2 \times 10^{-6}$, computed from the second-order fit, was applied to derive the susceptibility of bone as $\chi_{bone} = \Delta\chi + \chi_{Gd\text{-}DTPA} = -10.9 \times 10^{-6}$, which is in good agreement with the value of $-11.3 \times 10^{-6}$ reported previously for bovine bone measured by a susceptibility matching technique (*30*).

### *Rabbit Specimen*

Although the long-range goal of the current work was to provide a means of investigating the field distribution in human bone, the surface charge method was also evaluated with the rabbit specimen since the high bone volume fraction (0.60) and thick trabeculae are in sharp contrast to the structure of human radius trabecular bone, which is characterized by relatively low bone volume fraction (0.16 in the present specimen) and slender trabeculae with large intertrabecular spacing. In addition, the rabbit trabeculae, which are thick with respect to voxel size, facilitated the generation of accurate surface models for the field computations. Errors in the measured field map resulting from large-scale gradients were also minimized by resorting to a sample arrangement involving a container of susceptibility-matched glass as described under Methods (Fig. 8).

**TABLE 2**
**Determination of $\Delta\chi$ by Regression between the Measured and Predicted Field ($n$ = 12,540) for the Rabbit Specimen with the Anatomic Axis Parallel to the Applied Field**

| Order of background terms | $R^2$ | $p$ | $\Delta\chi$ | 95% Confidence interval for $\Delta\chi$ | |
|---|---|---|---|---|---|
| | | | | Lower | Higher |
| 0 | 0.73 | <0.0001 | $-2.45 \times 10^{-6}$ | $-2.42 \times 10^{-6}$ | $-2.48 \times 10^{-6}$ |
| 1 | 0.90 | <0.0001 | $-2.29 \times 10^{-6}$ | $-2.27 \times 10^{-6}$ | $-2.31 \times 10^{-6}$ |
| 2 | 0.91 | <0.0001 | $-2.32 \times 10^{-6}$ | $-2.30 \times 10^{-6}$ | $-2.33 \times 10^{-6}$ |

By inspection, there is good agreement between the cross sections of the measured and predicted field maps for both spatial orientations of the specimen (Figs. 9). The arrows in Figs. 9A and 9B point to field perturbations caused by trabeculae in adjacent slices. When the trabeculae become rotated such that they are nearly parallel to the applied field, the induced field becomes much more homogeneous (Figs. 9C and 9D). The surface charge method is thus shown to accurately model the effect of trabecular architecture on the induced field.

Since data collection was more optimal than for the human specimen, the computed field was a good predictor of measured values ($R^2 = 0.73$, $p < 0.0001$) for both spatial orientations of the specimen even when no background gradient terms were included in the regression (Tables 2 and 3). However, background gradients were still detectable, as shown by the significant correlation between the $z$ coordinate and the measured field (Fig. 10). In contrast to the strong relationship between the $x$ coordinate and the measured field in the human specimen (Fig. 6), the $R^2$ correlation coefficient was only 0.28 ($p < 0.0001$) since the short-range field gradients induced by the thick, closely spaced trabeculae were larger in comparison to the background gradient.

Inclusion of the terms representing linear (first-order) background gradients resulted in excellent fits for both spatial orientations of the specimen (Tables 2 and 3). As shown in Tables 2 and 3, incorporation of second-order background terms did not significantly improve the fits. Therefore, $\Delta\chi = -2.3 \times 10^{-6}$ and $\chi_{bone} = \Delta\chi + \chi_{Gd\text{-}DTPA} = -11.0 \times 10^{-6}$ were determined from the results of the first-order fits. As expected, the measured susceptibility was not affected by rotating the specimen even though the induced field, as shown in Fig. 9, was dependent on the spatial orientation of the bone. The similar results for the two orientations suggest that the susceptibility measurements are precise. Further, the derived value for $\chi_{bone}$ is also in excellent agreement with the value of $-11.3 \times 10^{-6}$ reported previously for powdered bovine bone (*30*).

## CONCLUSIONS

The surface charge method has been shown to accurately predict the induced magnetic field in comparison with field maps measured by asymmetric spin-echo pulse sequences. Further, the method was able to predict the susceptibility of trabecular bone from the coefficient of the regression between the computed and measured field values. The same technique could be applied to nondestructively determine the susceptibility of other materials in complex structures. The multipole-accelerated algorithm for computing the field from the surface charge density was also shown to be highly efficient. For example, the surface model of the rabbit femur specimen consisted of 150,010 triangular surface elements. In contrast, the field was computed at 5819 spatial locations per minute using a low-end laptop computer (133 MHz Pentium). Therefore, the results indicate the algorithm to be suitable for evaluating the relationship between trabecular structure and NMR line broadening. A goal of particular interest in this context is

**TABLE 3**
**Determination of $\Delta\chi$ by Regression between the Measured and Predicted Field ($n$ = 14,374) for the Rabbit Specimen with the Anatomic Axis Perpendicular to the Applied Field**

| Order of background terms | $R^2$ | $p$ | $\Delta\chi$ | 95% Confidence interval for $\Delta\chi$ | |
|---|---|---|---|---|---|
| | | | | Lower | Higher |
| 0 | 0.73 | <0.0001 | $2.48 \times 10^{-6}$ | $2.46 \times 10^{-6}$ | $2.51 \times 10^{-6}$ |
| 1 | 0.86 | <0.0001 | $2.28 \times 10^{-6}$ | $2.26 \times 10^{-6}$ | $2.30 \times 10^{-6}$ |
| 2 | 0.89 | <0.0001 | $2.26 \times 10^{-6}$ | $2.24 \times 10^{-6}$ | $2.28 \times 10^{-6}$ |

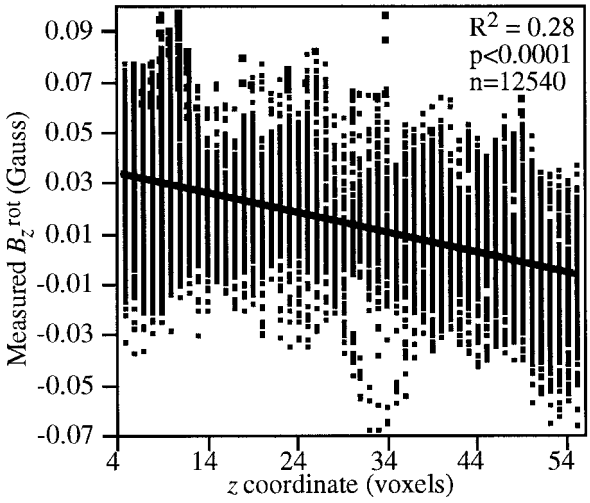


**FIG. 10.** The measured field in the rabbit specimen was significantly correlated with the $z$ coordinate, suggesting that background gradients were present even though a Shigemi tube was used. In contrast to the field in the human specimen (Fig. 6), the short-range fields induced by the trabeculae caused larger deviations from the large-scale background gradient indicated by the line of regression. The anatomic axis of the specimen was parallel to the applied field $B_0$.

to advance the understanding of structural changes resulting from disease processes such as osteoporosis and from response to treatment.

## ACKNOWLEDGMENTS

The authors gratefully acknowledge the assistance and expertise provided by Dr. Suzanne Wehrli in performing the NMR experiments and Dr. M. Takahashi for the acquisition of the rabbit specimen images. This work was supported by NIH Grants RO1 40671 and RO1 41443.

## REFERENCES

1. S. L. Hui, C. W. Slemenda, and C. C. Johnston, Jr., Baseline measurement of bone mass predicts fracture in white women, *Ann. Int. Med.* **111,** 355–361 (1989).
2. R. D. Wasnich, P. D. Ross, J. W. Davis, and J. M. Vogel, A comparison of single and multisite BMC measurements for assessment of spine fracture probability, *J. Nucl. Med.* **30,** 1166–1171 (1989).
3. P. D. Ross, J. W. Davis, J. M. Vogel, and R. D. Wasnich, A critical review of bone mass and the risk of fractures in osteoporosis, *Calcif. Tissue Int.* **46,** 149–161 (1990).
4. S. R. Cummings, D. M. Black, M. C. Nevitt, W. Browner, J. Cauley, K. Ensrud, H. K. Genant, L. Palermo, J. Scott, and T. M. Vogt, Bone density at various sites for prediction of hip fractures, *Lancet* **341,** 72–75 (1993).
5. M. Kleerekoper, A. R. Villanueva, J. Stanciu, D. Sudhaker Rao, and A. M. Parfitt, The role of three-dimensional trabecular microstructure in the pathogenesis of vertebral compression fractures, *Calcif. Tissue Int.* **37,** 594–597 (1985).
6. R. R. Recker, Architecture and vertebral fracture, *Calcif. Tissue Int.* **53**(Suppl. 1), S139–142 (1993).
7. C. L. Gordon, C. E. Webber, N. Christoforou, and C. Nahmias, *In vivo* assessment of trabecular bone structure at the distal radius from high-resolution magnetic resonance images, *Med. Phys.* **24,** 585–593 (1997).
8. S. Majumdar, H. K. Genant, S. Grampp, D. C. Newitt, V. H. Truong, J. C. Lin, and A. Mathur, Correlation of trabecular bone structure with age, bone mineral density, and osteoporotic status: *In vivo* studies in the distal radius using high resolution magnetic resonance imaging, *J. Bone Miner. Res.* **12,** 111–118 (1997).
9. F. W. Wehrli, S. N. Hwang, J. Ma, H. K. Song, J. C. Ford, and J. G. Haddad, Noninvasive assessment of cancellous bone volume and structure in the forearm by magnetic resonance microimaging and image processing, *Radiology* **206,** 347–357 (1998).
10. F. W. Wehrli, J. C. Ford, M. Attie, H. Y. Kressel, and F. S. Kaplan, Trabecular structure: Preliminary application of MR interferometry, *Radiology* **179,** 615–621 (1991).
11. S. Majumdar and H. K. Genant, In vivo relationship between marrow T2* and trabecular bone density determined with a chemical shift-selective asymmetric spin-echo sequence, *J. Magn. Reson. Imaging* **2,** 209–219 (1992).
12. C. H. Durney, J. Bertolina, D. C. Ailion, R. Christman, A. G. Cutillo, A. H. Morris, and S. Hashemi, Calculation and interpretation of inhomogeneous line broadening in models of lungs and other heterogeneous structures, *J. Magn. Reson.* **85,** 554–570 (1989).
13. J. A. Bertolina, C. H. Durney, D. C. Ailion, A. G. Cutillo, A. H. Morris, and K. C. Goodrich, Experimental verification of inhomogeneous line-broadening calculations in lung models and other inhomogeneous structures, *J. Magn. Reson.* **99,** 161–169 (1992).
14. J. C. Ford, F. W. Wehrli, and H. Chung, Magnetic field distribution in models of trabecular bone, *Magn. Reson. Med.* **29,** 373–379 (1993).
15. D. A. Yablonskiy and E. M. Haacke, Theory of NMR signal behavior in magnetically homogeneous tissues: The static dephasing regime, *Magn. Reson. Med.* **32,** 749–763 (1994).
16. D. A. Yablonskiy, W. R. Reinus, H. Stark, and E. M. Haacke, Quantitation of $T_2'$ anisotropic effects on magnetic resonance bone mineral density measurement, *Magn. Reson. Med.* **36,** 214–221 (1996).
17. K. Selby, S. Majumdar, D. C. Newitt, and H. K. Genant, Investigation of MR decay rates in microphantom models of trabecular bone, *J. Magn. Reson. Imaging* **6,** 549–559 (1996).
18. S. N. Hwang and F. W. Wehrli, The calculation of the susceptibility-induced magnetic field from 3D NMR images with applications to trabecular bone, *J. Magn. Reson. B* **109,** 126–145 (1995).
19. H. Chung, F. W. Wehrli, and S. Wehrli, Three-dimensional nuclear magnetic resonance microscopy of trabecular bone, *J. Bone Miner. Res.* **10,** 1452–1461 (1995).
20. H. Chung, S. N. Hwang, H. N. Yeung, and F. W. Wehrli, Mapping of the magnetic field distribution in cancellous bone, *J. Magn. Reson. B* **113,** 172–176 (1996).
21. W. T. Dixon, Simple proton spectroscopic imaging, *Radiology* **153,** 189–194 (1984).
22. K. Sekihara, S. Matsui, and H. Kohno, A new method of measuring static field distribution using modified Fourier NMR imaging, *J. Phys. E Sci. Instrum.* **18,** 224–227 (1985).
23. H. Jara, F. W. Wehrli, and H. Chung, High-resolution variable flip angle 3D MR imaging of trabecular microstructure *in vivo, Magn. Reson. Med.* **29,** 528–539 (1993).
24. A. R. Bogdan and P. M. Joseph, RASEE: A rapid spin-echo pulse sequence, *Magn. Reson. Imaging* **8,** 13–19 (1990).

*25.* S. N. Hwang, F. W. Wehrli, and J. L. Williams, Probability-based structural parameters from three-dimensional nuclear magnetic resonance images as predictors of trabecular bone strength, *Med. Phys.* **24,** 1255–1261 (1997).

*26.* I. Beichl and F. Sullivan, Making connections, *IEEE Computat. Sci. Eng.* **3,** 9–12 (1996).

*27.* K. Nabors, S. Kim, and J. White, Fast capacitance extraction of general three-dimensional structures, *IEEE Trans. Micro. Theory Tech.* **40,** 1496–1506 (1992).

*28.* R. S. Elliot, The local field, *in* "Electromagnetics: History, Theory, and Applications," pp. 410–411, IEEE Press, Piscataway, 1993.

*29.* S. C. K. Chu, Y. Xu, J. I. Balschi, and C. S. Springer, Bulk magnetic susceptibility shifts in NMR studies of compartmentalized samples: Use of paramagnetic reagents, *Magn. Reson. Med.* **13,** 239–262 (1990).

*30.* J. A. Hopkins and F. W. Wehrli, Magnetic susceptibility measurement of insoluble solids by NMR: Magnetic susceptibility of bone, *Magn. Reson. Med.* **37,** 494–500 (1997).

*31.* G. W. Smith, Diamagnetic susceptibilities of organic compounds, *in* "CRC Handbook of Chemistry and Physics" (R. C. Weast and M. J. Astle, Eds.), pp. E123–E131, CRC Press, Boca Raton, FL, 1982.

*32.* Physical constants of inorganic compounds, *in* "CRC Handbook of Chemistry and Physics" (R. C. Weast, and M. J. Astle, Eds.), pp. B72–B166, CRC Press, Boca Raton, FL, 1982.

*33.* L. Josephson, J. Bigler, and D. White, The magnetic properties of some materials affecting MR images, *Magn. Reson. Med.* **22,** 204–208 (1991).

*34.* R. M. Weisskoff and S. Kiihne, MRI susceptometry: Image-based measurement of absolute susceptibility of MR contrast agents and human blood, *Magn. Reson. Med.* **24,** 375–383 (1992).

*35.* J. Weis, S. Nilsson, A. Ericsson, M. Wikström, G. O. Sperber, and A. Hemmingsson, Measurement of magnetic susceptibility and MR contrast agent concentration, *Magn. Reson. Imaging* **12,** 859–864 (1994).